

# JGR Solid Earth

## RESEARCH ARTICLE

10.1029/2024JB029562

### Key Points:

- We identify a pair of 2019 Ridgecrest earthquake aftershocks at 10 km depth with reverse polarity P and S wavetrains at several stations
- The events are about 115 m apart and have opposing focal mechanisms with fault planes 10–20° different in orientation
- These results can be explained by either locally low effective fault friction or, more likely, strong short-wavelength stress heterogeneity

### Supporting Information:

Supporting Information may be found in the online version of this article.

### Correspondence to:

P. M. Shearer,  
pshearer@ucsd.edu

### Citation:

Shearer, P. M., Shabikay Senobari, N., & Fialko, Y. (2024). Implications of a reverse polarity earthquake pair on fault friction and stress heterogeneity near Ridgecrest, California. *Journal of Geophysical Research: Solid Earth*, 129, e2024JB029562. <https://doi.org/10.1029/2024JB029562>

Received 21 MAY 2024

Accepted 14 OCT 2024

### Author Contributions:

**Conceptualization:** Peter M. Shearer, Yuri Fialko

**Formal analysis:** Yuri Fialko

**Funding acquisition:** Peter M. Shearer

**Investigation:** Nader Shabikay Senobari, Yuri Fialko

**Methodology:** Peter M. Shearer, Nader Shabikay Senobari, Yuri Fialko

**Software:** Peter M. Shearer,

Nader Shabikay Senobari




**Supervision:** Peter M. Shearer

**Writing – original draft:** Peter M. Shearer, Yuri Fialko

© 2024. The Author(s).

This is an open access article under the terms of the [Creative Commons Attribution-NonCommercial-NoDerivs License](https://creativecommons.org/licenses/by/4.0/), which permits use and distribution in any medium, provided the original work is properly cited, the use is non-commercial and no modifications or adaptations are made.

# Implications of a Reverse Polarity Earthquake Pair on Fault Friction and Stress Heterogeneity Near Ridgecrest, California

Peter M. Shearer<sup>1</sup> , Nader Shabikay Senobari<sup>2</sup> , and Yuri Fialko<sup>1</sup> 

<sup>1</sup>Scripps Institution of Oceanography, UC San Diego, La Jolla, CA, USA, <sup>2</sup>Department of Computer Science and Engineering, UC Riverside, Riverside, CA, USA

**Abstract** We apply the Matrix Profile algorithm to 100 days of continuous data starting 10 days before the 2019 M 6.4 and M 7.1 Ridgecrest earthquakes from borehole seismic station B921 near the Ridgecrest aftershock sequence. We identify many examples of reversely polarized waveforms, but focus on one particularly striking earthquake pair with strongly negatively correlated P and S waveforms at B921 and several other nearby stations. Waveform-cross-correlation-based relocation of these events indicates they are at about 10 km depth and separated by only 115 m. Individual focal mechanisms are poorly resolved for these events because of the limited number of recording stations with unambiguous P polarities. However, relative P and S polarity and amplitude information can be used to constrain the likely difference in fault plane orientation between the two events to be 5–20°. We explore possible models to explain these observations, including low effective coefficients of fault friction and short-wavelength stress heterogeneity caused by prior earthquakes. Although definitive conclusions are lacking, we favor local stress heterogeneity as being more consistent with other observations for the Ridgecrest region.

**Plain Language Summary** Earthquake focal mechanisms are estimated from seismic observations and provide valuable information on fault geometry and crustal stress orientation at depth. Most focal mechanisms are spatially correlated, that is, mechanisms tend to be similar to those of neighboring earthquakes. However, on rare occasions earthquake pairs are observed that appear nearly opposite in orientation, as evidenced by seismograms that are flipped in polarity. These extreme examples of focal mechanism diversity are valuable because they provide strong constraints on fault and stress properties at depth. Here we identify and study a particularly well-recorded reverse-polarity earthquake pair among aftershocks of the 2019 M6.4 and M7.1 earthquakes at Ridgecrest, California. Our analysis shows that they are at 10 km depth in the crust but only 115 m apart and that their fault planes differ in orientation by less than 20°. This implies either unusually low values of fault friction, which permit faults to slip even when they are far from their optimal faulting orientation, or strong changes in stress orientation at depth, perhaps caused by residual stresses from prior earthquakes.

## 1. Introduction

Earthquake focal mechanisms provide important constraints on stress orientation at depth. While a single mechanism provides only limited information, a group of focal mechanisms of varying orientation can be used to invert for the principal stress direction, assuming uniform stress across the source region (e.g., Gephart & Forsyth, 1984; Michael, 1987). In general, greater focal mechanism diversity will provide tighter constraints on stress orientation and may also place limits on the effective coefficient of friction during faulting. For example, many aftershock zones following the 1989 Loma Prieta, California, earthquake contained widely divergent mechanisms, which Michael et al. (1990) interpreted as indicating an extremely heterogeneous stress field resulting from a near-total stress drop of the Loma Prieta mainshock. In contrast, Beroza and Zoback (1993) and Zoback and Beroza (1993) argued that the Loma Prieta focal mechanism diversity was consistent with a nearly uniform uniaxial stress field with principal stress axis almost normal to the mainshock fault plane and very low effective coefficients of fault friction.

Nakamura (1978) used cross-spectra to identify inverted polarity records in the A<sub>1</sub> deep moonquake cluster. More recently, the widespread use of waveform cross-correlation to characterize and relocate earthquakes has led to the discovery of “reverse-polarity” earthquake pairs with seismograms of nearly opposite polarity (see recent review by Cesca et al., 2024). Prieto et al. (2012) identified examples of reverse polarity waveforms from five or more

Writing – review & editing: Peter M. Shearer, Nader Shabikay Senobari, Yuri Fialko

stations for events in the Bucaramanga earthquake nest at ~160-km depth in Colombia. Ma and Wu (2013) found five doublets among 2631 aftershocks of the 2008 Wenchuan, China, earthquake with flipped polarity on all three components of a nearby station. Trugman et al. (2020) detected 45 “antisimilar” earthquake pairs among ~30,000 aftershocks of the 2019 Ridgecrest, California, mainshocks, with interevent separations of hundreds of meters. In the same Ridgecrest aftershock sequence, Wang and Zhan (2020) used moment tensor analysis to identify two pairs of reverse polarity mechanisms with hypocenter separations of 2–4 km.

These reverse-polarity earthquake pairs are valuable as extreme examples of focal mechanism diversity, but it is not yet clear how much local stress heterogeneity they require or if they can be explained entirely with low effective coefficients of fault friction. To address these issues, we apply the Matrix Profile (MP) algorithm (Shabikay Senobari et al., 2024) to 100 days of continuous data (starting 10 days before the 2019 M 6.4 Ridgecrest earthquake) from a nearby borehole seismometer. We find many examples of anti-correlated waveforms, including a particularly striking pair at about 10 km depth with nearly identical polarity-flipped P and S waveforms, which became the focus of this paper. Our analysis shows that the earthquakes in this reverse-polarity pair are located only 115 m apart with fault planes that likely differ in orientation by 10–20°. We explore the implications of this result for local stress heterogeneity and fault friction.

## 2. Data Analysis

The 4–5 July 2019 M 6.4 and M 7.1 Ridgecrest mainshocks generated a vigorous aftershock sequence with tens of thousands of events detected in the first few months (e.g., Plesch et al., 2020). To detect reverse polarity waveforms during this time period, we obtained 100 days of continuous data from the vertical component of borehole station B921 (see Figure 1) extending from 10 days before to 90 days after the M 6.4 event. We applied a 1–10 Hz bandpass filter and downsampled to 20 samples/s. We modified the Matrix Profile (MP) algorithm (Shabikay Senobari et al., 2024) to output the minimum rather than the maximum value of the correlation coefficient of every 5-s segment with the rest of the time series. As described in Shabikay Senobari et al. (2024), the MP provides an efficient way to perform template matching without templates, that is to cross-correlate everything with everything. This has the advantage of detecting even the tiniest event pairs that cross-correlate, even if neither event is contained in an existing catalog.

From the MP output for station B921, we searched for times when the correlation coefficient was less than  $-0.95$  for at least 2 s and found many examples of anti-correlated waveform segments (see Figure 2). Note that the anti-correlated pulse shapes are distinctive enough that the negative correlations could not have resulted from cycle-skipping of positively correlated pulses (see discussion on p. 7 of Cesca et al., 2024). Most of the example pairs we identified were of anti-correlated P-waves, with the corresponding S-waves showing little or no correlation (either positive or negative). This result differs from the observations of Ma and Wu (2013) for Wenchuan aftershocks, who found reversed polarity S-waves but not P-waves and Trugman et al. (2020) who plot many examples of anti-correlated S-waves for Ridgecrest aftershock pairs. We suspect that the dominance of anti-correlated P-waves in our analysis may result from our selection criteria, which tends to favor anti-correlation of the initial part of the P and S wavetrain.

It is interesting to note the large difference in magnitude between many of our anti-correlated P-wave event pairs. For example, the top pair of events in Figure 2 have catalog magnitudes of 3.5 and 1.3 and we find a P-wave amplitude ratio at B921 of about 100. The bottom pair of events is the most extreme, with magnitudes of 3.7 and 0.7 and a P-wave amplitude ratio at B921 of about 2600. These results are similar to those observed for Parkfield repeating earthquakes by Nadeau et al. (1995) who found highly correlated waveforms for a micro-earthquake cluster with an observed amplitude range of more than 40 (see their Figure 1). Good correlation of large-event waveforms with those of smaller events occurs because their apparent pulse widths are similar, a result of both attenuation and the 1- to 10-Hz bandpass filter we apply to the data. In our case, the Cajon Pass borehole results of Abercrombie (1995) suggest corner frequencies of 2–10 Hz for M 3.7 earthquakes, corresponding to source durations of about 0.03–0.16 s, which are less than or roughly equal to the pulse durations seen in Figure 2.

Although most of our reverse polarity observations were of P-waves alone, we found one particularly striking example of a reverse polarity earthquake pair, which contains both P- and S-waves with flipped polarity. The waveforms for this pair are plotted in Figure 3, showing the B921 waveforms as well as data from other stations that also show anti-correlated waveforms. Note that this pair is not among the 45 antisimilar Ridgecrest

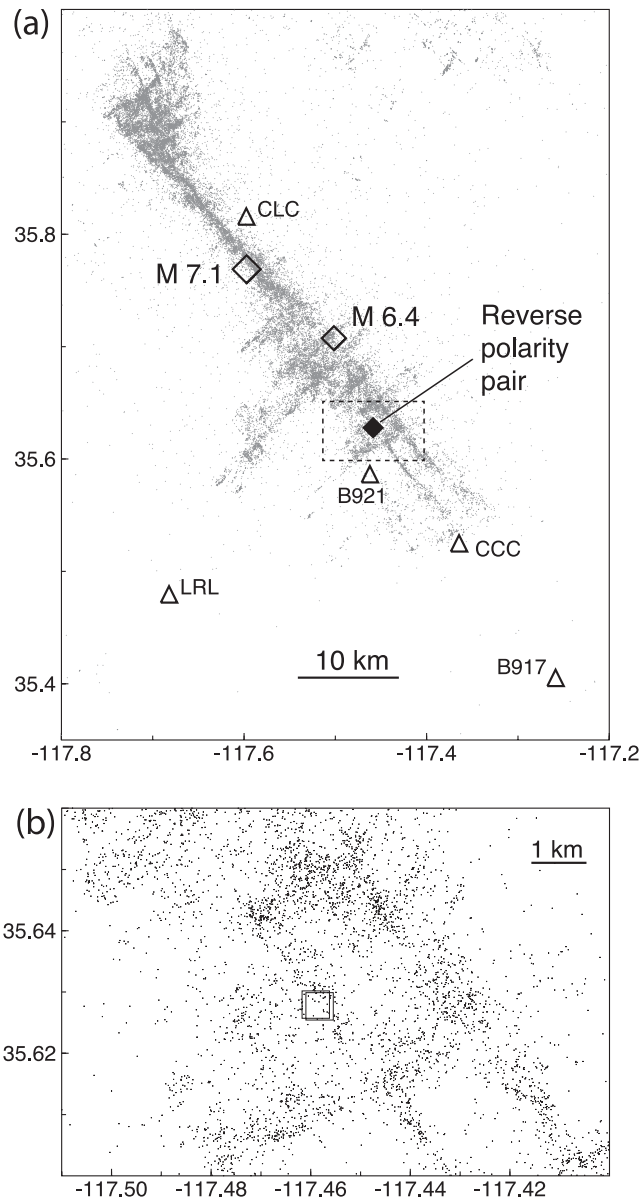


**Figure 1.** (a) A map showing the locations of the 4 July M 6.4 and 5 July M 7.1 Ridgecrest mainshocks, catalog seismicity in 2019 (gray dots), station locations (triangles), and the reverse polarity earthquake pair that is the focus of our analysis. (b) A closeup of the region outlined in the dashed rectangle in the top map, showing the epicenters of the reverse polarity pair as squares.

arrival times all within 0.64 s of the observed picks, with most residuals less than 0.2 s. This relocation step is critical for our analysis because the original catalog location is off by over 15 km.

The second event is much smaller than the first event (note a factor of 8–19 amplitude difference between the two events in Figure 3) and its phase arrivals are less clear. However, waveform cross-correlation of the traces shown in Figure 3 gives 12 differential P and S times that can be used to compute relative event locations for the pair, which we perform using the DIFLOC subroutine from the GrowClust algorithm (Trugman & Shearer, 2017). This yields final locations of (35.62765, -117.45822, 9.9076 km) and (35.62795, -117.45899, 9.9924 km) for the two events, which are separated by only 115 m. The resulting differential time residuals are all less than 0.01 s. Bootstrap resampling of the differential times gives one standard error limits for the separation distance of 108

earthquake pairs previously identified by Trugman et al. (2020), who used a multi-station approach based on waveform cross-correlation of known events and required at least five negative correlations of  $-0.85$  or less from separate P- and S-wave 1.5-s windows. In contrast, our method is applied to data from a single station and requires a negative correlation of  $-0.95$  or less over a 5-s window. Because we examine continuous data, we are not limited to known events and indeed many of our detected events are not in the SCSN catalog. Detection of anti-correlated events using focal mechanism analysis, waveform cross-correlation, template matching, and the MP algorithm is a rich area for future research.

Here, we focus on the pair shown in Figure 3 rather than perform a more comprehensive analysis of all our reverse-polarity observations at station B921 for the following reasons.

1. Trugman et al. (2020) has already shown that 45 anti-correlated pairs are widely distributed among Ridgecrest aftershocks and Wang and Zhan (2020) identified two pairs of  $M > 3.5$  earthquakes near the Ridgecrest mainshock epicenters with nearly opposite focal mechanisms. Adding more examples of anti-correlated pairs, while of some value, will not necessarily contribute as much to our understanding as exploring the implications of a single well-constrained pair in detail.
2. The tightest constraints on local fault properties and stress heterogeneity are provided by pairs of events at the shortest separation distances and with the most anti-correlated focal mechanisms. Because our target event pair has both anti-correlated P- and S-waves at several stations, it is possible to obtain precise differential locations and limits on allowed focal mechanism differences.
3. Other examples of reverse polarity waveforms we found for station B921 contained only anti-correlated P-waves and thus are unlikely to be as closely located as our target event pair.
4. More detailed analysis of other pairs requires obtaining waveforms from other stations and performing waveform cross-correlation, a process that may be difficult to automate, given the errors in the catalog location that we found for one of our target events (see below).

The two events occurred on 10 July at 22:47:20 and 22 July at 12:37:19. The earlier event is associated with a M 0.96 SCSN catalog event with cuspid 38524287 and location: lat = 35.7623, lon = -117.5617, depth = 11.80 km, time = 22:47:17.48. However, examining waveforms for this earthquake showed that some SCSN phase identifications were incorrect owing to the presence of other earthquakes occurring at similar times. Careful hand picking of P and S arrivals at 16 stations and application of the COMLOC location algorithm (Lin & Shearer, 2006) yields a solution (lat = 35.6278, lon = -117.4586, depth = 9.95 km, time = 22:47:19.98) that predicts P and S

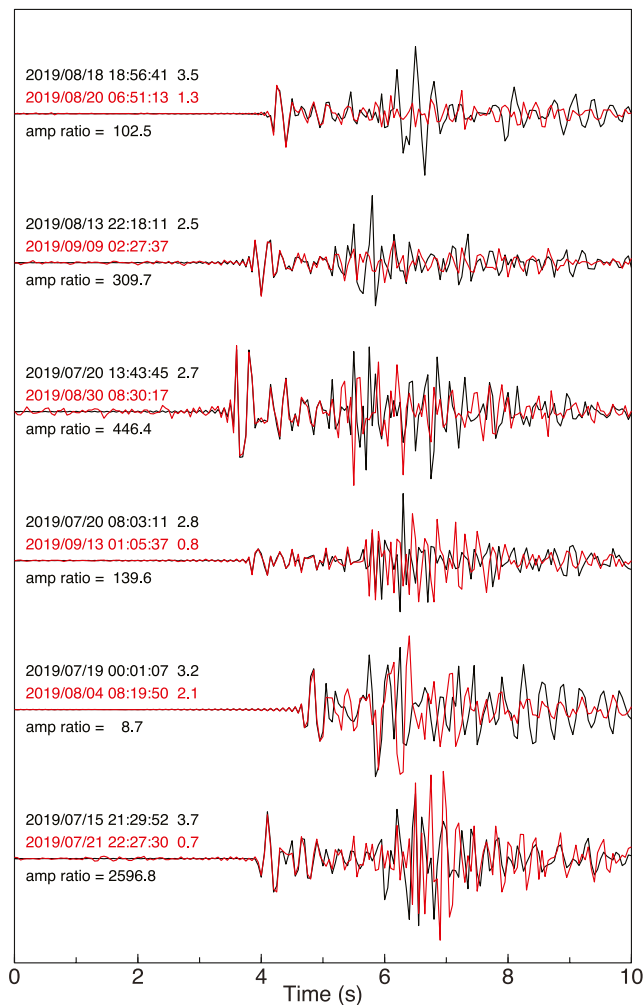


**Figure 2.** Reverse polarity records from station B921 identified using the Matrix Profile algorithm. Six earthquake pairs are plotted with the red trace flipped in polarity to show its negative correlation with the black trace for the first 2 seconds of the wavetrain (i.e., the P-wave arrival). Trace alignment is from the MP results. The black trace is normalized to the same maximum amplitude and the red trace is scaled to match the P-wave amplitude. The red-to-black trace P-wave amplitude ratio is labeled. Corresponding date/times are indicated above the traces. Events associated with earthquakes in the SCSN catalog have magnitudes listed to the right of the date/time.

focal mechanism pair within the allowed set and compute its predicted differential P and S amplitude ratios at these stations. We consider acceptable fits to achieve at least a 50% reduction in log amplitude ratio misfit RMS compared to a single amplitude scaling factor between the events.

Examples of focal mechanism pairs that meet this criteria are plotted in Figure 4 and show that both strike-slip and oblique-slip mechanisms are possible, given the limited P-polarity information. Histograms showing the number of pairs as a function of the angular separation between the fault planes and the difference in fault strikes are shown in Figure 5a. Both nodal planes are used to compute these angular differences. The best-fitting focal mechanism pairs achieve log amplitude ratio misfit reductions of 60%–70% and span angular separations from 2° to 20°, with many at 10° to 15° separation. Somewhat wider angular separations are permitted when only a 50% reduction in log amplitude ratio misfit is required, as shown by the small number of solutions beyond 20° separation in Figure 5a. Out of the 336 total solution pairs (listed in the supplement), there are three pairs with angular separations of 30° to 34°, each with a misfit reduction close to 50%. However, we don't necessarily expect perfect fits to the differential amplitude observations, given that directivity effects may cause amplitude variations

and 131 m. Note that separate locations for the two events are visible in Figure 1b and trend along an azimuth of about N65° W, which crudely agrees with a local alignment of the aftershock seismicity.

We focus for the remainder of this paper on this specific earthquake pair because of its strong anti-correlation of both P and S at several stations, which allow us to compute a precise differential location, and, as explained below, constrain differences in the event focal mechanisms. In the future, we hope to more thoroughly explore the other reverse-polarity waveform pairs contained in the MP results, which may help to expand the set of anti-correlated events cataloged by Trugman et al. (2020), particularly if we relax the  $-0.95$  correlation coefficient cutoff.

## 2.1. Focal Mechanism Analysis

We found that there are too few records with clear P-wave polarities to accurately determine a focal mechanism for either event in the anti-correlated earthquake pair. However, we can use the differential amplitude information from our cross-correlation results to place limits on how “opposite” the mechanisms are, that is, the angular separation between the inferred slip planes. Our approach is related to the use of relative P polarities from waveform cross-correlation by Shelly et al. (2016) and relative polarities and S/P amplitude ratios by Shelly et al. (2023) to estimate focal mechanisms within clusters of earthquakes and is very similar to the strategy of Cheng et al. (2023) to combine P polarities with P and S amplitude ratios to perform a joint focal mechanism inversion for event clusters that minimizes the differences between observed and radiation-pattern-predicted amplitude ratios between focal mechanism pairs.

Our analysis works as follows.

1. For the larger, earlier event, we hand-pick P polarities for stations with clear and unambiguous onsets, that is, stations CCC, CLC, B917, and B921, all of which have up (positive) P-wave first motions.
2. We use the HASH algorithm (Hardebeck & Shearer, 2002; Skoumal et al., 2024) to return a large set (13,716) of focal mechanisms consistent with positive polarities at these four stations.
3. We obtain observed P and S amplitude ratios using waveform cross-correlation at stations B917, B921, CCC, CLS, and LRL. These ratios are labeled in Figure 3 and generally agree between the components at the same station but vary somewhat among the different recording stations, suggesting that the focal mechanisms are not perfectly reversed (assuming no directivity amplitude variations). Next, we consider every possible

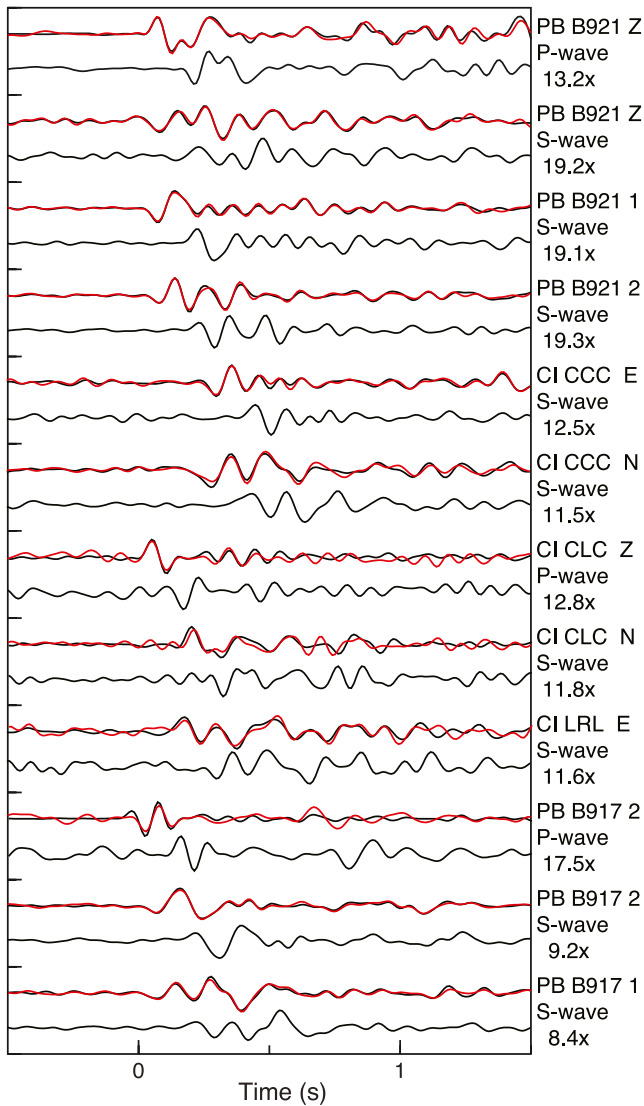


**Figure 3.** P and S waveform comparison for the reverse polarity earthquake pair. The top trace in each pair shows the 10 July event in black and 22 July event in red (aligned with flipped polarity). The bottom trace in each pair shows the 22 July event with its original polarity. Station network, name, and component are labeled at right. Records are bandpass filtered at 1–10 Hz. Amplitudes are self-normalized with the second-event amplitude increased by the indicated scaling factor (e.g., 13.2 for the top record pair) to match the first event.

not predicted by double-couple radiation patterns. Thus we consider that the results constrain the fault planes of the two events to be between  $0^\circ$  and  $25^\circ$  apart, with a  $5^\circ$  to  $20^\circ$  separation being most likely. Figure 5b plots the difference in fault strike between the first and second event for the allowed focal mechanism pairs (event 2 strike minus event 1 strike). The average strike difference is near zero, with a spread between about  $-15^\circ$  and  $+15^\circ$ . Much of the angular difference (Figure 5a) is thus likely due to a small difference in dip angles.

### 3. Discussion

Reversed or nearly reversed focal mechanisms have been observed in comparisons between pre-mainshock events and those following large ruptures, such as the 2011 Tohoku-oki earthquake (e.g., Hardebeck & Okada, 2018; Hasegawa et al., 2012; Ide et al., 2011; Yagi & Fukahata, 2011), and have been attributed to a near-total stress drop for the mainshock and/or dynamic overshoot. Large stress rotations caused by mainshock slip have also been observed for the 1992 Landers earthquake (Hauksson, 1994) and the 2002 Denali earthquake (Ratchkovski, 2003). Wang and Zhan (2020) identified two pairs of nearly reverse-polarity mechanisms among  $M_L > 3.5$  Ridgecrest aftershocks, which are close to epicenters of the M 6.4 and 7.1 Ridgecrest events. Wang and Zhan (2020) noted that the identified reverse-polarity pairs are located near regions of high coseismic slip, and suggested that they result from dynamic overshoot. However, given that both of the events in our anti-correlated earthquake pair occurred after the M 7.1 mainshock and the events are only about  $\sim 100$ -m apart, dynamic overshoot due to the mainshock cannot account for their reverse polarity. One might argue for dynamic overshoot produced by the first event of the reverse-polarity pair, thus locally reversing the stress orientation for the second event. However, the likelihood of overshoot is low for small events and can be ruled out as the cause of the reverse polarity for our anti-correlated earthquake pair because the distance between the events greatly exceeds their estimated dimensions (less than 40 m for the larger event, assuming a stress drop of 3 MPa or higher), implying negligible stress interactions.

More viable explanations include those discussed in the introduction, in which previous studies have attributed extreme aftershock focal mechanism diversity to heterogeneity in either stress and/or fault strength (e.g., Beroza & Zoback, 1993; Michael et al., 1990; Zoback & Beroza, 1993). For our reverse polarity pair, these possibilities can be evaluated in light of the very small separation of the event hypocenters (115 m) and the opposing slip that occurs on fault planes that differ in angular orientation by less than  $25^\circ$ . In the following analysis, we assume that the sense of fault slip is the same as the sense of resolved shear stress on a slip interface prior to the earthquake occurrence.

#### 3.1. Homogeneous Background Stress

The close spatial proximity of the two events might be used to argue that they occurred under the same background stress. Under the assumption of a locally homogeneous stress, both the orientation and magnitude of principal stresses are the same at each hypocenter. If so, the opposite polarity implies that (a) nodal planes of the two events are distinct (i.e., the angle between them is neither  $0^\circ$  nor  $90^\circ$ ); (b) the principal stresses are almost parallel to one of the nodal planes (and almost perpendicular to the other nodal plane) for each event; and (c) the maximum compression axis is in the extensional quadrant of a focal mechanism for each event. Figure 6 illustrates the respective rupture orientations, assuming that both events are predominantly strike-slip. In case of a substantial dip-slip component, the maximum compressive stress is sub-vertical rather than sub-horizontal, and

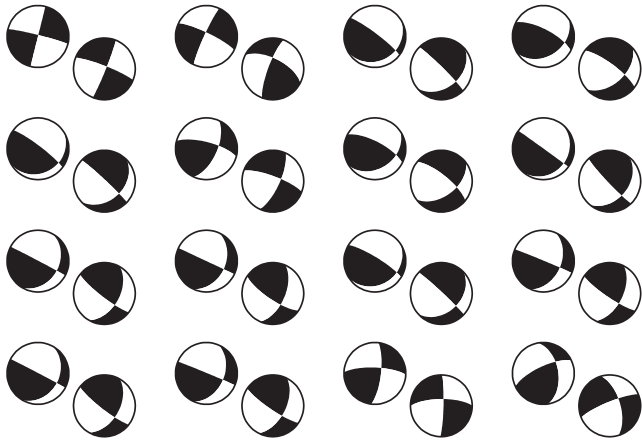


**Figure 4.** Sixteen examples of focal mechanism solutions for the Ridgecrest reverse polarity earthquake pair for that satisfy the available P-wave polarity data and achieve at least a 50% reduction in RMS misfit to the available differential P and S amplitudes. In each pair, the earlier and larger event is plotted on the lower right in its relative map-view location with respect to the later event to the northwest.

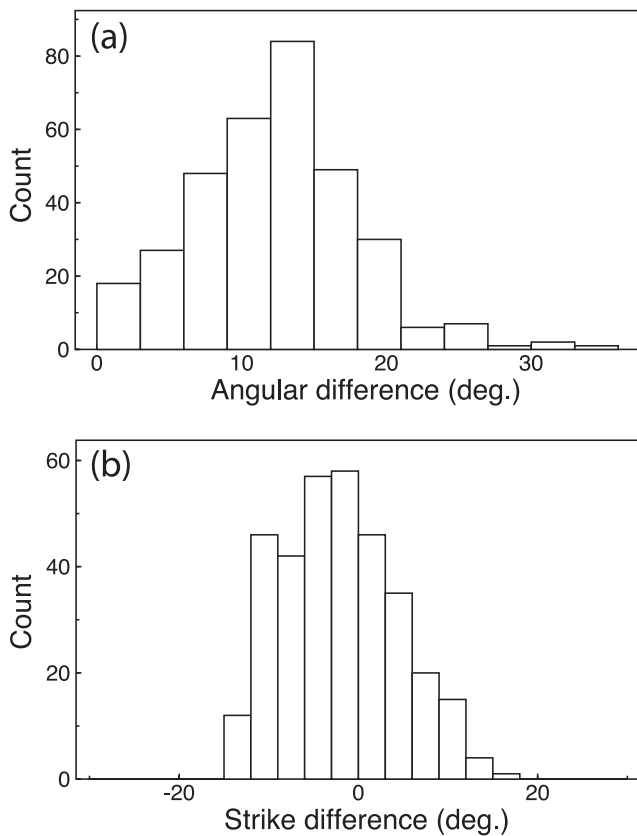


**Figure 5.** (a) For the Ridgecrest reverse polarity earthquake pair, a histogram of focal mechanism solution pairs that satisfy the available P-wave polarity data and achieve at least a 50% reduction in RMS misfit to the available differential P and S amplitudes from waveform cross-correlation, plotted as a function of the angular separation between the two fault planes. (b) A histogram of permitted fault strike differences between the two events.

the analysis presented below still applies. We note that the assumed configuration (Figure 6) may be consistent with the regional stress field. Taking the determined event locations at face value, the azimuth from the second (more westerly) event to the first one is  $\sim 116^\circ$ . Near-coincident nodal planes of the two events allow one to use the relative event locations to infer the absolute orientation of the nodal planes, and thus approximate orientations of the principal stress axes ( $\sim 116^\circ$  and  $\sim 26^\circ$ ). Accounting for uncertainties, these orientations are close to those of the minimum and maximum horizontal compression axes in the Ridgecrest area (e.g., Fialko & Jin, 2021; Yang & Hauksson, 2013). We also note that conditions (a) and/or (c) above would be inconsistent with the assumption of a locally homogeneous stress if the strike difference between the two fault planes is equal to, or less than zero (Figure 5b). We therefore proceed considering the case of a small but positive difference in strike angles, such that the nodal planes of the second event have larger strike angles compared to those of the first event, as depicted in Figure 6.

A near-orthogonal orientation of the nodal planes with respect to the principal stress axes requires the respective faults to be extremely weak, as the shear stress resolved on slip planes becomes vanishingly small for  $\theta_1 \rightarrow 0$  and  $\theta_2 \rightarrow 90^\circ$  (Figure 6). Such a weakness can be attributed to a low coefficient of friction  $\mu$ , high pore fluid pressure  $p$ , or some combination of the two. Fault friction can be low either statically or dynamically. Because strong dynamic weakening is thought to require sufficiently large displacements and slip rates (e.g., Brown & Fialko, 2012; Di Toro et al., 2011; Rice, 2006), it is unlikely activated during small earthquakes (e.g., Fialko, 2021). To place constraints on the static coefficient of friction, we consider the state of stress in the hypocentral region of the reverse polarity events.

We assume that one of the principal stresses is vertical and lithostatic,  $\sigma_{lith} = -\rho_r gz$ , and the pore pressure is hydrostatic,  $p = \rho_w gz$ , where  $z$  is depth (positive downward),  $g$  is the gravitational acceleration, and  $\rho_r$  and  $\rho_w$  are the densities of rock and water, respectively. Occurrence of both strike-slip and normal earthquakes in the Ridgecrest area indicates a transtensional stress regime (e.g., Jin & Fialko, 2020; Yang & Hauksson, 2013), so that the maximum ( $\sigma_1$ ) and intermediate ( $\sigma_2$ ) compressive stresses have similar magnitudes,  $\sigma_1 \approx \sigma_2 = \sigma_{Hmax} = \sigma_{lith}$ , and the least compressive stress ( $\sigma_3$ ) is horizontal (Fialko, 2021). The lower bound on the magnitude of the effective least compressive stress (the least compressive stress less the pore pressure) is given by the Mohr-Coulomb failure envelope for normal faulting (e.g., Sibson, 1974),

$$\sigma'_3 = -\frac{(\rho_r - \rho_w)gz}{K}, \quad (1)$$

where

$$K = \left(\sqrt{1 + \mu^2} + \mu\right)^2 \quad (2)$$

is the lateral Earth pressure coefficient. Orientations of small seismically active faults in the Ridgecrest area suggest an in situ coefficient of friction  $\mu = 0.4 - 0.6$ , with high-end values corresponding to optimally oriented faults, consistent with Byerlee's law (Fialko, 2021). Figure 7 shows the corresponding state of stress at depth of 10 km.

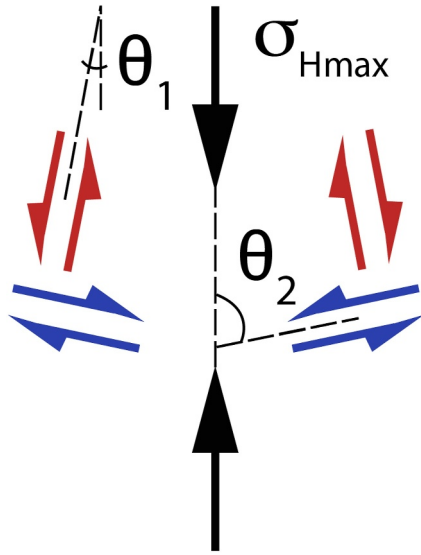


**Figure 6.** Admissible orientations of fault planes of the reverse polarity events under the assumption of a homogeneous stress. Blue and red arrows denote potential fault planes and sense of slip. Black arrows denote the axis of the maximum horizontal compressive stress  $\sigma_{Hmax}$ . Potential fault planes are at angles  $\pm\theta_1$  (red arrows) and  $\pm\theta_2$  (blue arrows) to  $\sigma_{Hmax}$  axis. Angle  $\theta_1$  is close to 0, and angle  $\theta_2$  is close to  $90^\circ$ .

The coefficient of friction that enables slip on sub-optimally oriented faults depends on the fault orientation with respect to the principal stresses. The angular difference between the reverse polarity faults provides an upper bound on the angle between the fault plane and the maximum compressive stress axis. Given the maximum admissible difference in strike angles of  $\sim 10\text{--}15^\circ$  (Figure 5b), we consider a particular case of  $\theta_1 = 90^\circ - \theta_2 = 6^\circ$ , which corresponds to the compression axis approximately bisecting the dihedral angle formed by conjugate fault pairs (red and blue arrows in Figure 6). This yields the coefficient of friction of 0.22 for the reverse polarity faults that are sub-parallel to the maximum compression axis (red arrows in Figure 6), and 0.07 for faults that are nearly orthogonal to the maximum compression axis (blue arrows in Figure 6). Relaxing the assumption of fault plane symmetry about the  $\sigma_{Hmax}$  axis (Figure 6) would result in a small increase in the estimated coefficient of friction for one of the two faults, but a decrease for the other. The estimated values of the coefficient of friction on the reverse polarity faults will be lower still, for example, for a smaller difference in strike angles (Figure 5b), larger than assumed magnitude of the effective least compressive stress  $|\sigma'_3|$ , and/or non-negligible cohesion (fault strength at zero normal stress).

Next, we consider the possibility that the reverse polarity faults are weakened due to high pore fluid pressure. An elevated (above hydrostatic) pore pressure cannot explain activation of severely mis-oriented faults in the presence of faults of different orientations, as faults that are more optimally oriented will be activated first. We therefore consider a case of pre-existing faults of a

certain orientation in relatively intact host rocks. Given the maximum and minimum effective principal stresses  $\sigma'_1$  and  $\sigma'_3$ , respectively, a condition for activation of a pre-existing fault is (Sibson, 1985):

$$\frac{\sigma'_3}{\sigma'_1} = \frac{1 - \mu \tan \theta}{1 + \mu \cot \theta}, \quad (3)$$

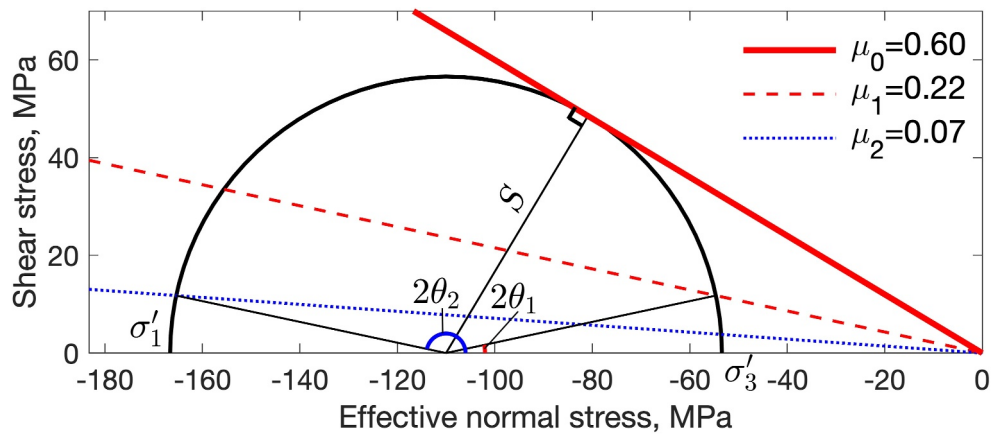


**Figure 7.** Assumed state of stress in the hypocentral region of the reverse polarity events. Black curve (the Mohr circle) denotes variations in shear stress on potential slip planes as a function of fault orientation. Radius of the Mohr circle represents the maximum shear stress,  $S = |\sigma'_1 - \sigma'_3|/2$ . Red solid line is the Mohr-Coulomb failure envelope corresponding to slip on pre-existing optimally oriented faults for the coefficient of friction  $\mu_0 = 0.6$ . Cohesion on the fault interface is assumed to be negligible. Angles  $\theta_1$  and  $\theta_2$  correspond to orientations of the reverse polarity faults with respect to the maximum horizontal compressive stress (Figure 6). The ratio of shear stress to the effective normal stress at the intersections between thin black lines and the Mohr circle gives the coefficients of friction,  $\mu_1$  and  $\mu_2$ , for the correspondingly oriented faults. Dashed red and blue lines denote failure envelopes for faults that are nearly parallel and nearly orthogonal to the maximum compressive stress, respectively (see Figure 6). Calculations assume  $z = 10$  km,  $\rho_c = 2.7 \times 10^3$  kg/m<sup>3</sup>,  $\rho_w = 10^3$  kg/m<sup>3</sup>,  $g = 9.8$  m/s<sup>2</sup>,  $\theta_1 = 6^\circ$  and  $\theta_2 = 84^\circ$ .

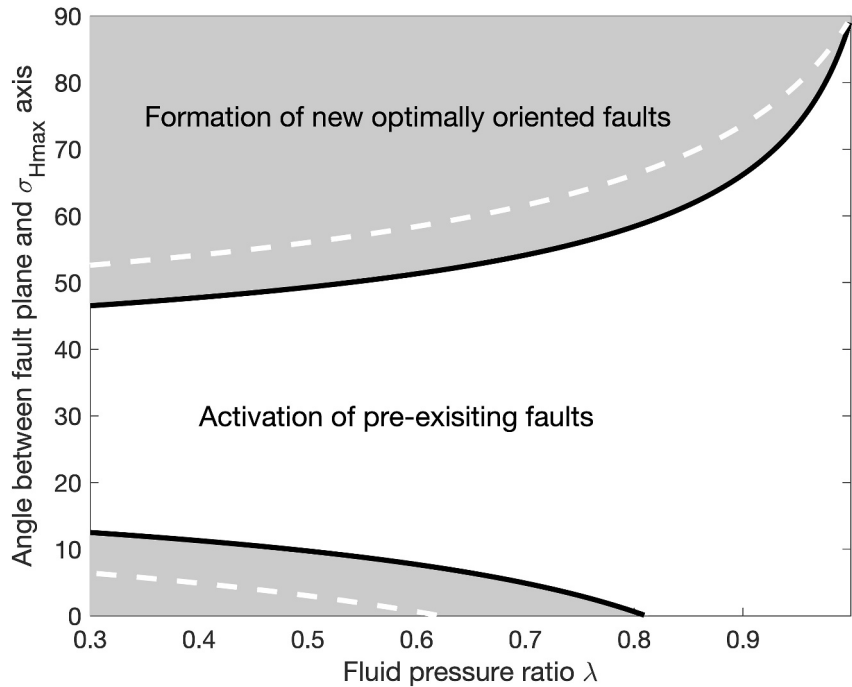


**Figure 8.** Orientations of faults that can be re-activated by increases in pore fluid pressure, as a function of the fluid pressure ratio  $\lambda$ . Re-activation is prohibited in the shaded areas, where criteria for the formation of new (optimally oriented) faults are first met. Black solid lines demarcate the parameter space of fault re-activation, assuming uniaxial compressive strength of the “intact” rocks  $C = 50$  MPa. White dashed lines correspond to  $C = 100$  MPa. Hydrostatic pore pressure corresponds to  $\lambda \approx 0.4$ . Calculations use  $\mu = 0.6$  and  $z = 10$  km.

where  $\theta$  is the angle between the fault plane and the maximum compression axis. Equation 3 gives rise to the following expression for the differential stress:

$$\sigma'_1 - \sigma'_3 = \mu \frac{\tan \theta + \cot \theta}{1 + \mu \cot \theta} \sigma'_1. \quad (4)$$

The Mohr-Coulomb criterion for failure of intact rock (i.e., formation of new faults) in terms of the effective principal stresses is

$$\sigma'_1 = -C + K\sigma'_3, \quad (5)$$

where  $C$  is the uniaxial compressive strength of rocks, and  $K$  is given by Equation 2. Equation 5 can be written as

$$\sigma'_1 - \sigma'_3 = -\frac{C}{K} + \left(1 - \frac{1}{K}\right)\sigma'_1. \quad (6)$$

Assuming that the maximum compressive stress is lithostatic,  $\sigma'_1 = -\rho_r g z (1 - \lambda)$ , where  $\lambda$  is the fluid pressure ratio (for hydrostatic fluid pressure,  $\lambda = \rho_w / \rho_r$ ), Equations 4 and 6 can be combined to relate the fault orientation  $\theta$  to the fluid pressure ratio  $\lambda$  for the transtensional stress regime:

$$\lambda = 1 - \frac{1 + \mu \cot \theta}{\mu K (\tan \theta + \cot \theta)} \frac{C}{\rho_r g z}. \quad (7)$$

The long-term uniaxial compressive strength of crystalline rocks  $C$  is of the order of 100 MPa (e.g., Price, 2016). Figure 8 shows the magnitude of fluid overpressure necessary to activate pre-existing faults while preventing creation of new optimally oriented faults, for  $C = 50$  MPa (black solid contours) and  $C = 100$  MPa (white dashed



contours). Smaller values of  $C$  result in a narrower range of fault orientations that admit re-shear. As one can see from Figure 8, faults that are sub-parallel to the maximum compression axis ( $\theta < 10^\circ$ ) can be activated with relatively modest increases in the pore fluid pressure above the hydrostatic value ( $\lambda > 0.4$ ). Activation of faults that are at high angles to the maximum compression axis requires fluid pressure approaching the lithostatic value ( $\lambda \rightarrow 1$ ). High pore fluid pressures raise a possibility of hydrofracture. The latter can be initiated if the least compressive stress becomes tensile, and exceeds the intrinsic tensile strength (of the order of several megapascals for common rock types, e.g. Fialko & Rubin, 1997). This condition is never met for the range of parameters explored in Figure 8, even at near-lithostatic values of pore fluid pressure. This is because both the least and maximum principal stresses approach the lithostatic level as the pore pressure increases.

We argue that neither very low friction nor a chronic over-pressurization of the host rocks are a likely explanation for the observed reverse polarity events. Analysis of orientations of active faults in the Ridgecrest region indicates that most faults are consistent with an in situ coefficient of friction of 0.4–0.6 (Fialko, 2021), well above the values of 0.1–0.2 inferred for the reverse polarity faults under the assumption of a locally homogeneous stress. Low friction and/or high fluid pressure cannot be widespread throughout the seismogenic zone because they would make the crust extremely weak and unable to support deviatoric stresses greater than several megapascals (Figure 7). Such a low strength of the bulk of the upper crust would be insufficient to maintain surface topography, and inconsistent with earthquake stress drops of several tens of megapascals commonly observed in the region (e.g., Shearer et al., 2022). Anomalously low friction and/or high pore fluid pressure might be unique to small isolated faults such as those that produced the reverse polarity events. However, we note that few rock types have coefficients of friction below 0.3 (e.g., water-saturated clays), and the respective rocks are typically velocity-strengthening (e.g., Moore & Lockner, 2007), that is, prone to creep rather than to stick-slip. In general, higher coefficients of friction tend to correlate with more unstable slip, and vice versa (e.g., Mitchell et al., 2015; Mitchell et al., 2016). A conditional slip stability is also promoted by high fluid pressure (low effective normal stress), especially for small faults (e.g., Dieterich, 1979). Thus near-lithostatic pore fluid pressure may help reduce the effective strength of severely mis-oriented faults, but at the same time suppress slip instabilities and thus seismic ruptures.

### 3.2. Heterogeneous Background Stress

An alternative possibility is that the stress field is not locally homogeneous, but varies considerably over length scales of the order of  $10^2$  meters (the inferred distance between hypocenters of the reverse polarity events). In this case, the fault planes do not need to be highly mis-oriented with respect to the principal stresses. Stress heterogeneity implies rotation of the principal stress axes, by as much as  $90^\circ$  (e.g., if the nodal planes of the two events are parallel, and each rupture is optimally oriented with respect to the local principal stress). Note that a locally homogeneous stress would not be able to cause slip on faults if the difference between their strike angles is equal to, or less than zero (Figure 5b), thus requiring variations in the state of stress over the respective distances.

Stress heterogeneity can result from several factors, including stress concentration at the fault tips (e.g., d'Alessio & Martel, 2004), heterogeneous fault slip (e.g., Rice, 1993; Smith & Heaton, 2011), slip on non-planar faults (Dieterich & Smith, 2009; Lindsey et al., 2014), and variations in the mechanical properties of the host rocks (Barbot et al., 2009; Bedford et al., 2022; Fialko et al., 2002). At small wavelengths of tens to hundreds of meters, large spatial variations in stress are most likely due to stress concentration at the fault tips, or arrested fronts of earthquake ruptures propagating along pre-existing faults.

We quantify rotation of the principal stress axes at the fault tip using a model of an in-plane (Mode II) non-singular shear crack in an elastic medium (Fialko, 2015). We use the background stress field illustrated in Figure 7, and assume that the crack plane is optimally oriented with respect to the principal stress axes. The background (“far-field”) shear stress resolved on the crack plane is  $\sigma_0 \approx 49$  MPa (Figure 7). Fault slip reduces stress on the fault surface to some residual level  $\sigma_d$ , with  $\Delta\sigma = \sigma_0 - \sigma_d$  representing the static stress drop. A stress singularity at the crack tip is prevented by a thin process zone having length  $R$ . Within the process zone, we assume the Mohr-Coulomb yield stress,

$$\sigma_s = \sigma_c - \mu\sigma'_n, \quad (8)$$

where  $\sigma_c$  is the cohesive stress, and  $\sigma'_n$  is the effective normal stress. The cohesive stress  $\sigma_c$  is related to the uniaxial compressive strength  $C$  (Equation 5) as  $\sigma_c = 0.5C/\sqrt{K}$  (e.g., Twiss & Moores, 1992, p. 214). The short-term compressive strength measured in the lab is higher than the long-term compressive strength of the crust (Price, 2016). Because the former is likely more appropriate for arresting propagating ruptures, the magnitudes of the cohesive stress and the long-term compressive strength may be similar. We use  $\sigma_c = 70$  MPa in the subsequent analysis. Note that for the assumed background stress and crack orientation,  $-\mu\sigma'_n = \sigma_0$ .

Within the process zone, slip gradually increases from zero to the critical slip-weakening displacement  $D_c$ . The work done to evolve the shear stress from  $\sigma_s$  to  $\sigma_d$  is  $(\sigma_s - \sigma_d)D_c$ , referred to as the fracture energy. The crack half-length is  $L$ , of which  $F = L - R$  is the half-length of the developed part of the crack on which the shear stress is equal to  $\sigma_d$  (see Figure 4 in Fialko, 2015). The cohesive, background, and residual stresses are related to the crack length as follows:

$$\frac{\sigma_s - \sigma_0}{\sigma_s - \sigma_d} = \frac{2}{\pi} \arcsin \exp\left(-\frac{L_c}{F}\right), \quad (9)$$

where

$$L_c = \frac{\pi D_c}{4(1 - \nu)} \frac{G}{\sigma_s - \sigma_d} \quad (10)$$

is the process zone length in the limit of small-scale yielding ( $F \approx L \gg R$ ). In Equation 10,  $\nu$  is the Poisson ratio. An exact expression for the process zone length is

$$R = F \left( \exp \frac{L_c}{F} - 1 \right). \quad (11)$$

The along-crack slip distribution is given by Equation 33 in Fialko (2015, note a typo:  $\sigma_0$  should read  $\sigma_s$ ). The magnitude of stress perturbations at the crack tip scales with the stress drop  $\Delta\sigma$ , while the wavelength of stress perturbations scales with the process zone size  $R$ . Stress gradients are maximized by increasing the stress drop  $\sigma_0 - \sigma_d$ , and/or the strength drop  $\sigma_s - \sigma_d$ . In the following example, we use  $\sigma_d = 0.1\sigma_0$  (i.e., nearly complete stress drop), and  $D_c = 0.1$  m (suggested by seismic data, e.g., Tinti et al., 2004). For typical elastic moduli of rocks ( $G = 30$  GPa and  $\nu = 0.25$ ), these parameters give rise to  $R \approx 30$  m,  $L \approx 170$  m, and  $\Delta\sigma \approx 44$  MPa. An earthquake with the respective rupture size and stress drop would have a moment magnitude  $M_w \approx 3.8$ .

The total stress in the surrounding medium is given by the sum of the assumed background stress and the stress change due to a crack. To calculate the stress change from a crack, we approximate the along-crack slip distribution with an array of  $N$  finite edge dislocations, each having length  $L/N$ . For each dislocation, the Burger's vector is equal to the amount of slip calculated at the mid-point of the respective dislocation. A finite edge dislocation can be represented by a superposition of two semi-infinite in-plane edge dislocations of opposite sign. Analytical expressions for stresses due to a semi-infinite edge dislocation in a homogeneous elastic medium are readily available (e.g., Landau & Lifshitz, 1970, p. 130). The dislocation model is accurate at distances greater than the size of individual dislocations (i.e.,  $L/N$ ) off of the crack plane. In the examples presented below, we use  $N = 300$ .

Figure 9 shows the resulting stress field near the crack tip. The maximum compressive stress axis is rotated clockwise (away from the crack plane) in the extensional quadrant (below the crack plane), and counter-clockwise (toward the crack plane) in the compressional quadrant (above the crack plane). The maximum differential rotation is about 70–80°, with largest gradients across the crack plane. Colors denote an area where slip on pre-existing faults can be activated. For the given orientation of the principal stress axis  $\sigma'_1$ , we compute the shear and normal stresses resolved on potential slip planes that are optimally oriented with respect to  $\sigma'_1$ . The ratio of shear to normal stress normalized by the coefficient of friction denotes how close the material is to failure. Pre-existing optimally oriented faults would be activated if the normalized ratio is equal to, or greater than unity. Results shown in Figure 9 predict extensive off-fault yielding because the medium was already on the verge of failure prior to fault slip. In case of the intact medium (i.e., no pre-existing faults), off-fault yielding would involve

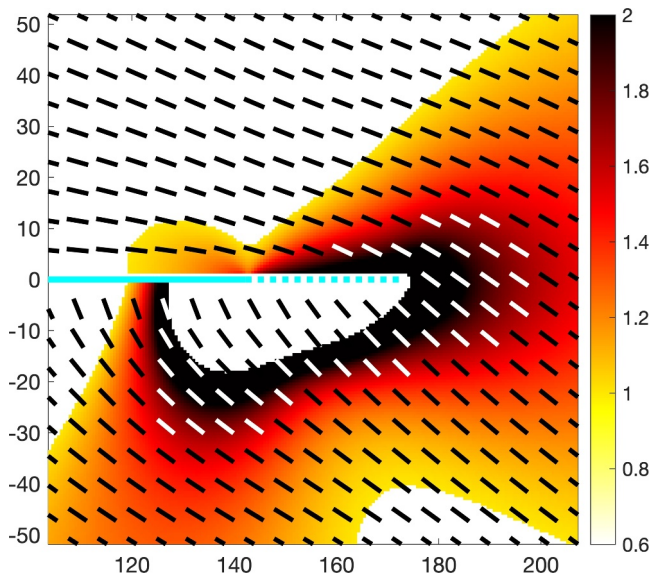


**Figure 9.** Stress field at the tip of a right-lateral Mode II shear crack. Black and white tick marks denote the orientation of the maximum compressive stress axis. Solid cyan line denotes the crack, and dashed cyan line denotes the process zone. Color represents the ratio of shear to normal stress divided by the assumed coefficient of friction (0.6). Shear and normal stresses are resolved on planes that are optimally oriented for failure according to the Mohr-Coulomb criterion. White area below the crack tip corresponds to positive  $\sigma_3$  (likely resulting in tensile fracturing). Axes numbers are in meters.

creation of new faults, and have a more limited extent due to cohesion (Equation 5). A number of simulations exploring a wide parameter range produced similar results (see Figures S1–S3 in Supporting Information S1). In particular, larger cracks and process zones increase the wavelength of stress perturbations at the crack tip, but result in smaller stress gradients. Varying the coefficient of friction changes the stress drop, but also the background stress, so that the ratio of stress perturbation to the background stress (which determines the amount of stress rotation) is not strongly affected. If the resolved shear stress is smaller (e.g., due to a non-optimal fault orientation), and/or the stress drop is a smaller fraction of the resolved shear stress, the amount of rotation of the principal stress axes is proportionally reduced (e.g., Fialko, 2021).

Results shown in Figure 9 do not exhibit large (up to  $90^\circ$ ) stress rotations over distances of  $\sim 10^2$  meters. However, it is conceivable that such rotations could be achieved by for example, a superposition of several faults or rupture fronts. Also, larger process zones (e.g., due to larger slip-weakening distance  $D_c$ ) can produce stress rotations that extend over larger distances away from the fault plane (Figure S3 in Supporting Information S1). The magnitude and spatial extent of stress perturbations can be further increased in the case of dynamic rupture at near-limiting speeds (e.g., Dunham et al., 2011; Rice et al., 2005). We note that the reverse polarity events occurred within the fault zone of the 2019 M 7.1 mainshock (Figure 1), where a significant stress heterogeneity may be expected from aftershocks of the 2019 event, as well as prior seismicity. We also note that field measurements suggest the fault offset-to-length ratios  $O(10^{-2})$  (e.g., Cowie & Scholz, 1992), about a factor of 5 larger than that in our “nearly complete stress drop” model (Figure 9). The latter therefore may not provide an upper bound on the amount of stress

rotation near fault tips. The effective strains of  $\sim 10^{-2}$  associated with cumulative fault slip, however, imply extensive yielding off of the fault plane, which can ultimately moderate the amount of rotation of the principal stress axes. The same is true for stress perturbations due to slip on geometrically complex interfaces (Dieterich & Smith, 2009; Lindsey et al., 2014). While models of slip on non-planar faults predict large stress perturbations due to fault roughness (Dieterich & Smith, 2009; Fang & Dunham, 2013), including local reversals in the sign of the resolved Coulomb stress, such perturbations are likely relaxed by secondary faulting and the bulk off-fault plasticity as faults continue to accumulate slip. Stress concentrations due to passing rupture fronts and slip on geometrically complex interfaces are one of the primary contributors to the formation of fault damage zones (Cochran et al., 2009; Dieterich & Smith, 2009; Kaneko & Fialko, 2011).

An additional stress rotation within fault damage zones might result from a “plastic core” which supports smaller deviatoric stresses compared to the host rocks, and therefore can develop higher fluid pressures without reaching a condition for hydrofracture (Faulkner et al., 2007; Rice, 1992). The plastic core model was proposed to explain operation of mature faults that are highly mis-oriented with respect to the regional tectonic stress, and unlikely applies to the Ridgecrest rupture which occurred on a developing low-offset fault that is nearly optimally oriented with respect to the regional stress field (e.g., Fialko & Jin, 2021).

A high diversity in orientations of closely spaced faults was reported in previous studies (e.g., Fialko, 2021; Iio et al., 2017). For example, Iio et al. (2017) found diverse focal mechanisms on the scale of  $10^2$  m near the fault that produced the 1984 M 6.8 Western Nagano Prefecture Earthquake in Japan, and attributed it to a heterogeneous strength, although it is possible that local stress heterogeneity might be involved as well. Smith and Heaton (2011) proposed that stress in the seismogenic upper crust is stochastically heterogeneous at all scales. Our results lend support to the existence of substantial stress heterogeneities at spatial scales of tens to hundreds of meters, for example, due to stress concentration at the fault tips, in the near field of major faults due to stress perturbations from arrested rupture fronts, fault roughness, and secondary faulting. The same mechanism may explain diverse focal mechanisms of aftershocks observed in Ridgecrest (Trugman et al., 2020; Wang & Zhan, 2020) and elsewhere (Beroza & Zoback, 1993; Michael et al., 1990). Extreme stress heterogeneity is also known to exist at

micro scales because of the irregular nature of elementary contacts (e.g., Bowden & Tabor, 1954; Dieterich & Kilgore, 1994; Mitchell et al., 2013). The available data however seem to indicate that stresses can be spatially coherent in the bulk of the crust over length scales of kilometers to tens of kilometers (e.g., Fialko & Jin, 2021; Iio et al., 2017; Yang & Hauksson, 2013). This view is supported by the fact that events with nearly reversed polarity appear to be relatively rare, have small magnitudes (i.e., sample stresses variations over relatively short wavelengths), and are limited to the near field of major faults, as documented in this study, as well as in previous studies (e.g., Trugman et al., 2020; Wang & Zhan, 2020).

#### 4. Conclusions

We analyze seismic waveform data from the 2019 Ridgecrest, California, earthquake sequence, using the Matrix Profile algorithm. We identify a number of event pairs that produced anti-correlated waveforms. One pair has a particularly striking anti-correlation of both P- and S-waves observed on several seismic stations. The respective events are located near the rupture zone of the 2019 M 7.1 mainshock at depth of about 10 km, and are only ~100 m apart. We constrain the difference in orientation of the nodal planes of the two events to be less than 25°. A near-perfect reversal in polarity implies either extremely low effective strength or strong stress heterogeneity. In case of a locally homogeneous stress, fault orientations that are sub-parallel to the orientation of the maximum horizontal stress would require less extreme values of the coefficient of friction and pore fluid over-pressure compared to fault orientations that are nearly orthogonal to the maximum horizontal stress axis. This would imply that faults that produced the reverse polarity events are more likely sub-parallel, rather than co-planar. A combination of moderate over-pressurization (above hydrostatic, but well below lithostatic) and a reduced coefficient of friction could help explain the reverse polarity events without the need to appeal for extremely low values of the coefficient of friction. However, the occurrence of events within the fault zone (Figure 1) makes the assumption of isolated pre-existing over-pressurized faults in otherwise competent host rocks (Figure 8) unlikely. Thus, we favor heterogeneous stress models, in which local stress heterogeneities, perhaps caused by rupture fronts and fault roughness, produce stress rotations that can explain the reverse polarity events, especially in combination with heterogeneous fault strength.

#### Data Availability Statement

The waveform data, and catalogs used in this study are available from the Southern California Earthquake Data Center (SCEDC, 2013). The SCEDC and Southern California Seismic Network (SCSN) are funded through U.S. Geological Survey Grant G20AP00037 and SCEC. The COMPLOC location package is from Lin and Shearer (2006). The GrowClust location code is from Trugman and Shearer (2017). The HASH focal mechanism code is from Hardebeck and Shearer (2002). Matlab scripts used in calculating stresses due to a 2-D plane strain shear crack are provided in the supplement.

#### References

- Abercrombie, R. E. (1995). Earthquake source scaling relationships from 1 to 5 ML using seismograms recorded at 2.5-km depth. *Journal of Geophysical Research*, 100(B12), 24015–24036. <https://doi.org/10.1029/95jb02397>
- Barbot, S., Fialko, Y., & Sandwell, D. (2009). Three-dimensional models of elasto-static deformation in heterogeneous media, with applications to the Eastern California Shear Zone. *Geophysical Journal International*, 179(1), 500–520. <https://doi.org/10.1111/j.1365-246x.2009.04194.x>
- Bedford, J. D., Faulkner, D. R., & Lapusta, N. (2022). Fault rock heterogeneity can produce fault weakness and reduce fault stability. *Nature Communications*, 13(1), 326. <https://doi.org/10.1038/s41467-022-27998-2>
- Beroza, G. C., & Zoback, M. D. (1993). Mechanism diversity of the Loma Prieta aftershocks and the mechanics of mainshock-aftershock interaction. *Science*, 259(5092), 210–213. <https://doi.org/10.1126/science.259.5092.210>
- Bowden, F. B., & Tabor, D. (1954). *The friction and lubrication of solids*. Clarendon Press.
- Brown, K. M., & Fialko, Y. (2012). Melt wet mechanism of extreme weakening of gabbro at seismic slip rates. *Nature*, 488(7413), 638–641. <https://doi.org/10.1038/nature11370>
- Cesca, S., Niemi, P., Dahm, T., & Ide, S. (2024). Anti-repeating earthquakes and how to explain them. *Communications Earth & Environment*, 5(1), 158. <https://doi.org/10.1038/s43247-024-01290-1>
- Cheng, Y., Allen, R. M., & Taira, T. (2023). A new focal mechanism calculation algorithm (refoc) using inter-event relative radiation patterns: Application to the earthquakes in the Parkfield area. *Journal of Geophysical Research: Solid Earth*, 128(3), e2022JB025006. <https://doi.org/10.1029/2022jb025006>
- Cochran, E. S., Li, Y.-G., Shearer, P. M., Barbot, S., Fialko, Y., & Vidale, J. E. (2009). Seismic and geodetic evidence for extensive, long-lived fault damage zones. *Geology*, 37(4), 315–318. <https://doi.org/10.1130/g25306a.1>
- Cowie, P. A., & Scholz, C. H. (1992). Displacement-length scaling relationship for faults: Data synthesis and discussion. *Journal of Structural Geology*, 14(10), 1149–1156. [https://doi.org/10.1016/0191-8141\(92\)90066-6](https://doi.org/10.1016/0191-8141(92)90066-6)
- d'Alessio, M. A., & Martel, S. J. (2004). Fault terminations and barriers to fault growth. *Journal of Structural Geology*, 26(10), 1885–1896. <https://doi.org/10.1016/j.jsg.2004.01.010>

#### Acknowledgments

We thank the Editor and reviewers for their constructive comments and suggestions. This research was supported by the Southern California Earthquake Center (Contribution No. 13473). SCEC is funded by NSF Cooperative Agreement EAR-1600087 and USGS Cooperative Agreement G17AC00047. PMS acknowledges support from NSF (FAIN-2104240). NSS acknowledges support from NSF (FAIN-2103976). YF acknowledges support from NSF (EAR-1841273) and NASA (80NSSC22K0506).

- Dieterich, J. H. (1979). Modeling of rock friction I. Experimental results and constitutive equations. *Journal of Geophysical Research*, 84(B5), 2161–2168. <https://doi.org/10.1029/jb084ib05p02161>
- Dieterich, J. H., & Kilgore, B. D. (1994). Direct observation of frictional contacts: New insights for state-dependent properties. *Pure and Applied Geophysics*, 143(1–3), 283–302. <https://doi.org/10.1007/bf00874332>
- Dieterich, J. H., & Smith, D. E. (2009). Nonplanar faults: Mechanics of slip and off-fault damage. In *Mechanics, structure and evolution of fault zones* (pp. 1799–1815). Springer.
- Di Toro, G., Han, R., Hirose, T., De Paola, N., Nielsen, S., Mizoguchi, K., et al. (2011). Fault lubrication during earthquakes. *Nature*, 471(7339), 494–498. <https://doi.org/10.1038/nature09838>
- Dunham, E. M., Belanger, D., Cong, L., & Kozdon, J. E. (2011). Earthquake ruptures with strongly rate-weakening friction and off-fault plasticity, Part I: Planar faults. *Bulletin of the Seismological Society of America*, 101(5), 2296–2307. <https://doi.org/10.1785/0120100075>
- Fang, Z., & Dunham, E. M. (2013). Additional shear resistance from fault roughness and stress levels on geometrically complex faults. *Journal of Geophysical Research*, 118(7), 3642–3654. <https://doi.org/10.1002/jgrb.50262>
- Faulkner, D. R., Mitchell, T. M., Healy, D., & Heap, M. J. (2007). Slip on “weak” faults by the rotation of regional stress in the fracture damage zone. *Nature*, 444(7121), 922–925. <https://doi.org/10.1038/nature05353>
- Fialko, Y. (2015). Fracture and frictional mechanics - theory. In *Treatise on geophysics*, G. Schubert (Ed.), 2nd ed., Vol. 4 (pp. 73–91). <https://doi.org/10.1016/b978-044452748-6.00062-6>, Elsevier Ltd.
- Fialko, Y. (2021). Estimation of absolute stress in the hypocentral region of the 2019 Ridgecrest, California, earthquakes. *Journal of Geophysical Research*, 126(7), e2021JB022000. <https://doi.org/10.1029/2021jb022000>
- Fialko, Y., & Jin, Z. (2021). Simple shear origin of the cross-faults ruptured in the 2019 Ridgecrest earthquake sequence. *Nature Geoscience*, 14(7), 513–518. <https://doi.org/10.1038/s41561-021-00758-5>
- Fialko, Y., & Rubin, A. (1997). Numerical simulation of high pressure rock tensile fracture experiments: Evidence of an increase in fracture energy with pressure? *Journal of Geophysical Research*, 102(B3), 5231–5242. <https://doi.org/10.1029/96jb03859>
- Fialko, Y., Sandwell, D., Agnew, D., Simons, M., Shearer, P., & Minster, B. (2002). Deformation on nearby faults induced by the 1999 Hector Mine earthquake. *Science*, 297(5588), 1858–1862. <https://doi.org/10.1126/science.1074671>
- Gephart, J. W., & Forsyth, D. W. (1984). An improved method for determining the regional stress tensor using earthquake focal mechanism data: Application to the San Fernando earthquake sequence. *Journal of Geophysical Research*, 89(B11), 9305–9320. <https://doi.org/10.1029/jb089i11p09305>
- Hardebeck, J. L., & Okada, T. (2018). Temporal stress changes caused by earthquakes: A review. *Journal of Geophysical Research: Solid Earth*, 123(2), 1350–1365. <https://doi.org/10.1002/2017jb014617>
- Hardebeck, J. L., & Shearer, P. M. (2002). A new method for determining first-motion focal mechanisms [Software]. *Bulletin of the Seismological Society of America*, 92(6), 2264–2276. <https://doi.org/10.1785/0120010200>
- Hasegawa, A., Yoshida, K., Asano, Y., Okada, T., Inuma, T., & Ito, Y. (2012). Change in stress field after the 2011 great Tohoku-Oki earthquake. *Earth and Planetary Science Letters*, 355, 231–243. <https://doi.org/10.1016/j.epsl.2012.08.042>
- Hauksson, E. (1994). State of stress from focal mechanisms before and after the 1992 Landers earthquake sequence. *Bulletin of the Seismological Society of America*, 84(3), 917–934. <https://doi.org/10.1785/bssa0840030917>
- Ide, S., Baltay, A., & Beroza, G. C. (2011). Shallow dynamic overshoot and energetic deep rupture in the 2011 m w 9.0 Tohoku-Oki earthquake. *Science*, 332(6036), 1426–1429. <https://doi.org/10.1126/science.1207020>
- Iio, Y., Yoneda, I., Sawada, M., Miura, T., Katao, H., Takada, Y., et al. (2017). Which is heterogeneous, stress or strength? An estimation from high-density seismic observations. *Earth Planets and Space*, 69(1), 1–16. <https://doi.org/10.1186/s40623-017-0730-3>
- Jin, Z., & Fialko, Y. (2020). Finite slip models of the 2019 Ridgecrest earthquake sequence constrained by space geodetic data and aftershock locations. *Bulletin of the Seismological Society of America*, 110(4), 1660–1679. <https://doi.org/10.1785/0120200060>
- Kaneko, Y., & Fialko, Y. (2011). Shallow slip deficit due to large strike-slip earthquakes in dynamic rupture simulations with elasto-plastic off-fault response. *Geophysical Journal International*, 186(3), 1389–1403. <https://doi.org/10.1111/j.1365-246x.2011.05117.x>
- Landau, L. D., & Lifshitz, E. M. (1970). *Theory of elasticity* (2nd ed., p. 165). Pergamon Press.
- Lin, G., & Shearer, P. (2006). The COMLOC earthquake location package [Software]. *Seismological Research Letters*, 77(4), 440–444. <https://doi.org/10.1785/gssrl.77.4.440>
- Lindsey, E. O., Fialko, Y., Bock, Y., Sandwell, D. T., & Bilham, R. (2014). Localized and distributed creep along the southern San Andreas fault. *Journal of Geophysical Research*, 119(10), 7909–7922. <https://doi.org/10.1002/2014jb011275>
- Ma, X., & Wu, Z. (2013). Negative repeating doublets in an aftershock sequence. *Earth Planets and Space*, 65(8), 923–927. <https://doi.org/10.5047/eps.2013.01.006>
- Michael, A. J. (1987). Use of focal mechanisms to determine stress: A control study. *Journal of Geophysical Research*, 92(B1), 357–368. <https://doi.org/10.1029/jb092ib01p00357>
- Michael, A. J., Ellsworth, W. L., & Oppenheimer, D. H. (1990). Coseismic stress changes induced by the 1989 Loma Prieta, California earthquake. *Geophysical Research Letters*, 17(9), 1441–1444. <https://doi.org/10.1029/g1017i009p01441>
- Mitchell, E., Fialko, Y., & Brown, K. (2015). Frictional properties of gabbro at conditions corresponding to slow slip events in subduction zones. *Geochemistry, Geophysics, Geosystems*, 16(11), 4006–4020. <https://doi.org/10.1002/2015gc006093>
- Mitchell, E., Fialko, Y., & Brown, K. M. (2013). Temperature dependence of frictional healing of westerly granite: Experimental observations and numerical simulations. *Geochemistry, Geophysics, Geosystems*, 14(3), 567–582. <https://doi.org/10.1029/2012gc004241>
- Mitchell, E., Fialko, Y., & Brown, K. M. (2016). Velocity-weakening behavior of Westerly granite at temperature up to 600°C. *Journal of Geophysical Research*, 121(9), 6932–6946. <https://doi.org/10.1002/2016jb013081>
- Moore, D. E., & Lockner, D. A. (2007). Friction of the smectite clay montmorillonite: A review and interpretation of data. *The seismogenic zone of subduction thrust faults*, 317–345.
- Nadeau, R. M., Foxall, W., & McEvilly, T. (1995). Clustering and periodic recurrence of microearthquakes on the San Andreas fault at Parkfield, California. *Science*, 267(5197), 503–507. <https://doi.org/10.1126/science.267.5197.503>
- Nakamura, Y. (1978). A1 moonquakes-source distribution and mechanism. In *Lunar and planetary science conference proceedings* (Vol. 9, pp. 3589–3607).
- Plesch, A., Shaw, J. H., Ross, Z. E., & Hauksson, E. (2020). Detailed 3D fault representations for the 2019 Ridgecrest, California, earthquake sequence. *Bulletin of the Seismological Society of America*, 110(4), 1818–1831. <https://doi.org/10.1785/0120200053>
- Price, N. J. (2016). *Fault and joint development: In brittle and semi-brittle rock*. Elsevier.
- Prieto, G. A., Beroza, G. C., Barrett, S. A., López, G. A., & Florez, M. (2012). Earthquake nests as natural laboratories for the study of intermediate-depth earthquake mechanics. *Tectonophysics*, 570, 42–56. <https://doi.org/10.1016/j.tecto.2012.07.019>

- Ratchkovski, N. A. (2003). Change in stress directions along the central Denali fault, Alaska after the 2002 earthquake sequence. *Geophysical Research Letters*, *30*(19). <https://doi.org/10.1029/2003gl017905>
- Rice, J. R. (1992). Fault stress states, pore pressure distribution, and the weakness of the San Andreas Fault. In B. Evans & T. Wong (Eds.), *Fault mechanics and transport properties of rocks* (pp. 475–503). Academic.
- Rice, J. R. (1993). Spatio-temporal complexity of slip on a fault. *Journal of Geophysical Research*, *98*(B6), 9885–9907. <https://doi.org/10.1029/93jb00191>
- Rice, J. R. (2006). Heating and weakening of faults during earthquake slip. *Journal of Geophysical Research*, *111*(B5), B05311. <https://doi.org/10.1029/2005jb004006>
- Rice, J. R., Sammis, C. G., & Parsons, R. (2005). Off-fault secondary failure induced by a dynamic slip pulse. *Bulletin of the Seismological Society of America*, *95*(1), 109–134. <https://doi.org/10.1785/0120030166>
- SCEDC. (2013). Southern California earthquake Center [Dataset]. *Caltech*. <https://doi.org/10.7909/C3WD3xH1>
- Shabikay Senobari, N., Shearer, P. M., Funning, G. J., Zimmerman, Z., Zhu, Y., Brisk, P., & Keogh, E. (2024). The matrix profile in seismology: Template matching of everything with everything. *Journal of Geophysical Research: Solid Earth*, *129*(2), e2023JB027122. <https://doi.org/10.1029/2023jb027122>
- Shearer, P. M., Abercrombie, R. E., & Trugman, D. T. (2022). Improved stress drop estimates for M 1.5 to 4 earthquakes in southern California from 1996 to 2019. *Journal of Geophysical Research*, *127*(7), e2022JB024243. <https://doi.org/10.1029/2022jb024243>
- Shelly, D. R., Hardebeck, J. L., Ellsworth, W. L., & Hill, D. P. (2016). A new strategy for earthquake focal mechanisms using waveform-correlation-derived relative polarities and cluster analysis: Application to the 2014 Long Valley Caldera earthquake swarm. *Journal of Geophysical Research: Solid Earth*, *121*(12), 8622–8641. <https://doi.org/10.1002/2016jb013437>
- Shelly, D. R., Skoumal, R. J., & Hardebeck, J. L. (2023). Fracture-mesh faulting in the swarm-like 2020 Maacama sequence revealed by high-precision earthquake detection, location, and focal mechanisms. *Geophysical Research Letters*, *50*(1), e2022GL101233. <https://doi.org/10.1029/2022gl101233>
- Sibson, R. H. (1974). Frictional constraints on thrust, wrench and normal faults. *Nature*, *249*(5457), 542–544. <https://doi.org/10.1038/249542a0>
- Sibson, R. H. (1985). A note on fault reactivation. *Journal of Structural Geology*, *7*(6), 751–754. [https://doi.org/10.1016/0191-8141\(85\)90150-6](https://doi.org/10.1016/0191-8141(85)90150-6)
- Skoumal, R. J., Hardebeck, J. L., & Shearer, P. M. (2024). SKHASH: A Python package for computing earthquake focal mechanisms. *Seismological Research Letters*, *95*(4), 2519–2526. <https://doi.org/10.1785/0220230329>
- Smith, D. E., & Heaton, T. H. (2011). Models of stochastic, spatially varying stress in the crust compatible with focal-mechanism data, and how stress inversions can be biased toward the stress rate. *Bulletin of the Seismological Society of America*, *101*(3), 1396–1421. <https://doi.org/10.1785/0120100058>
- Tinti, E., Bizzarri, A., Piatanesi, A., & Cocco, M. (2004). Estimates of slip weakening distance for different dynamic rupture models. *Geophysical Research Letters*, *31*(2), L02611. <https://doi.org/10.1029/2003gl018811>
- Trugman, D. T., Ross, Z. E., & Johnson, P. A. (2020). Imaging stress and faulting complexity through earthquake waveform similarity. *Geophysical Research Letters*, *47*(1), e2019GL085888. <https://doi.org/10.1029/2019gl085888>
- Trugman, D. T., & Shearer, P. M. (2017). Growclust: A hierarchical clustering algorithm for relative earthquake relocation, with application to the Spanish Springs and Sheldon, Nevada, earthquake sequences [Software]. *Seismological Research Letters*, *88*(2A), 379–391. <https://doi.org/10.1785/0220160188>
- Twiss, R., & Moores, E. (1992). *Structural geology*. W.H. Freeman.
- Wang, X., & Zhan, Z. (2020). Seismotectonics and fault geometries of the 2019 Ridgecrest sequence: Insight from aftershock moment tensor catalog using 3-D Green's functions. *Journal of Geophysical Research: Solid Earth*, *125*(5), e2020JB019577. <https://doi.org/10.1029/2020jb019577>
- Yagi, Y., & Fukahata, Y. (2011). Rupture process of the 2011 Tohoku-Oki earthquake and absolute elastic strain release. *Geophysical Research Letters*, *38*(19), L19307. <https://doi.org/10.1029/2011gl048701>
- Yang, W., & Hauksson, E. (2013). The tectonic crustal stress field and style of faulting along the Pacific North America Plate boundary in Southern California. *Geophysical Journal International*, *194*(1), 100–117. <https://doi.org/10.1093/gji/ggt113>
- Zoback, M. D., & Beroza, G. C. (1993). Evidence for near-frictionless faulting in the 1989 (M 6.9) Loma Prieta, California, earthquake and its aftershocks. *Geology*, *21*(2), 181–185. [https://doi.org/10.1130/0091-7613\(1993\)021<0181:efnffi>2.3.co;2](https://doi.org/10.1130/0091-7613(1993)021<0181:efnffi>2.3.co;2)